Title

Decadal-scale variations in geomagnetic field intensity from ancient Cypriot slag mounds

Journal

Geochemistry, Geophysics, Geosystems, 16(1)

Authors

Shaar, R
Tauxe, L
Ben-Yosef, E
et al.

Publication Date

2015

DOI

10.1002/2014GC005455

Peer reviewed

AGU PUBLICATIONS

Geochemistry, Geophysics, Geosystems

RESEARCH ARTICLE
10.1002/2014GC005455

Special Section:
Magnetism From Atomic to Planetary Scales: Physical Principles and Interdisciplinary Applications in Geo- and Planetary Sciences

Key Points:
- Decadal-scale resolution paleointensity data from ancient slag mounds in Cyprus
- High paleointensity rate of change during the fifth century CE
- Levant and South Africa may be longitudinally paired active areas

Supporting Information:
- Readme
- MagIC_Readme
- Radiocarbon data
- Supplementary Material
- Table S3

Correspondence to:
R. Shaar,
ron.shaar@mail.huji.ac.il

Citation:
Shaar, R., L. Tauxe, E. Ben-Yosef, V. Kassianidou, B. Lorentzen, J. M. Feinberg, and T. E. Levy (2015), Decadal-scale variations in geomagnetic field intensity from ancient Cypriot slag mounds, *Geochem. Geophys. Geosyst.*, *16*, doi:10.1002/2014GC005455.

Received 11 JUN 2014
Accepted 20 DEC 2014
Accepted article online 5 JAN 2015

Decadal-scale variations in geomagnetic field intensity from ancient Cypriot slag mounds

Ron Shaar[1], Lisa Tauxe[1], Erez Ben-Yosef[1,2], Vasiliki Kassianidou[3], Brita Lorentzen[4], Joshua M. Feinberg[5,6], and Thomas E. Levy[7]

[1]Scripps Institution of Oceanography, University of California, San Diego, La Jolla, California, USA, [2]Department of Archaeology and Ancient Near Eastern Cultures, Tel Aviv University, Tel Aviv, Israel, [3]Department of History and Archaeology, University of Cyprus, Nicosia, Cyprus, [4]Cornell Tree-Ring Laboratory, Cornell University, Ithaca, New York, USA, [5]Department of Earth Sciences, Institute for Rock Magnetism, University of Minnesota, Minneapolis, Minnesota, USA, [6]Department of Anthropology, University of Minnesota, Minneapolis, Minnesota, USA, [7]Department of Anthropology, University of California, San Diego, La Jolla, California, USA

Abstract Geomagnetic models based on direct observations since the 1830s show that the averaged relative change in field intensity on Earth's surface over the past 170 years is less than 4.8% per decade. It is unknown if these rates represent the typical behavior of secular variations due to insufficient temporal resolution of archaeomagnetic records from earlier periods. To address this question, we investigate two ancient slag mounds in Cyprus—Skouriotissa Vouppes (SU1, fourth to fifth centuries CE, 21 m in height), and Mitsero Kokkinoyia (MK1, seventh to fifth centuries BCE, 8 m in height). The mounds are multilayered sequences of slag and charcoals that accumulated near ancient copper production sites. We modeled the age-height relation of the mounds using radiocarbon dates, and estimated paleointensities using Thellier-type IZZI experiments with additional anisotropy, cooling rate, and nonlinear TRM assessments. To screen out ambiguous paleointensity interpretations, we applied strict selection criteria at the specimen/sample levels. To ensure objectivity, consistency, and robust error estimation, we employed an automatic interpretation technique and put the data available in the MagIC database. The analyses yielded two independent subcentury-scale paleointensity time series. The MK1 data indicate relatively stable field at the time the mound accumulated. In contrast, the SU1 data demonstrate changes that are comparable in magnitude to the fastest changes inferred from geomagnetic models. We suggest that fast changes observed in the published archaeomagnetic data from the Levant are driven by two longitudinally paired regions, the Middle East and South Africa, that show unusual activity in geomagnetic models.

1. Introduction

Changes in the geomagnetic field that occur over short-time scales are referred to as geomagnetic secular variation (SV). One fundamental characteristic of SV, still not fully understood, concerns the shortest time scale for significant changes in field intensity. Direct measurements of field intensity that go back to 1832 [*Malin and Barraclough*, 1982] show relatively small changes with rather smooth behavior over decadal time scales [e.g., *Cafarella et al*., 1992; *Barraclough et al*., 2000]. In contrast, recent archaeomagnetic studies have revealed periods with significant intensity variations over decadal to centennial time scales [*Gallet et al*., 2003, *Ben-Yosef et al*., 2009; *Genevey et al*., 2009; *Shaar et al*., 2011; *Gómez-Paccard et al*., 2012]. This apparent inconsistency suggests that temporal variations in the geomagnetic field intensity over the past two centuries have been relatively small compared to earlier periods. To investigate this question, high-resolution paleointensity records from periods preceding those covered by direct geomagnetic observations are required.

Obtaining subcentury-scale paleointensity records is a difficult task. First, the studied material needs to fulfill a strict list of requirements [e.g., *Dunlop and Özdemir*, 2001; *Valet*, 2003; *Tauxe and Yamazaki*, 2007], such as having a pure thermoremanent magnetization (TRM) carried exclusively by stable single-domain (SD) like particles. In addition, paleointensity experiments should be carefully designed using sufficient number of specimens [*Paterson et al*., 2010], and with accurate corrections for remanence anisotropy [*Rogers et al*., 1979; *Selkin et al*., 2000; *Kovacheva et al*., 2009], cooling rate effects [e.g., *Genevey and Gallet*, 2002;

Ferk et al., 2014], and nonlinear TRM [*Selkin et al*., 2007; *Shaar et al*., 2010]. Furthermore, as the interpretations of the paleointensity experimental data can be nonunique a robust data analysis method is required to ensure comparability, objectivity, and robust assessment of error estimation [*Shaar and Tauxe*, 2013]. Finally, above all, achieving the desired resolution in age is difficult and often impossible.

This study pursues the challenge of obtaining subcentury-scale paleointensity records using ancient copper slag mounds [e.g., *Kassianidou*, 2004, *Levy et al*., 2008; *Ben-Yosef et al*., 2009; *Shaar et al*., 2011; *Ben-Yosef et al*., 2012]. Copper slag mounds are industrial waste mounds consisting of slag and charcoals (the main side product of copper smelting procedure) that accumulated as long as copper was produced in nearby smelting sites. Copper slag mounds afford a unique opportunity for obtaining virtually continuous high-resolution paleointensity time series.

The first paleointensity investigation of Levantine copper slag material was conducted by *Ben-Yosef et al*. [2008a, 2008b] who recognized the diversity of slag types, and demonstrated that some types of slag are suitable paleointensity source material. Based on this research, *Shaar et al*. [2010] examined the rock magnetic properties of selected slag material from Timna valley, Israel, and concluded that Timna's glassy slag contain populations of single domain (SD) like grains, ideal for paleointensity studies. Using synthetic remelted Fe-rich slag, *Shaar et al*. [2010] estimated the accuracy of the estimated field in paleointensity procedure on SD-like samples to be better than 6%. Later, *Shaar and Feinberg* [2013] demonstrated that the SD-like properties are due to submicrometer-scale dendritic structures in the ferromagnetic minerals. Based on these findings, *Ben-Yosef et al*. [2009] and *Shaar et al*. [2011] investigated contemporaneous slag mounds in Timna valley, Israel and in Khirbat En Nahas, Jordan, and constructed a decadal-scale paleointensity time series for the Iron Age.

In this study, we follow the approach presented in our previous studies, and investigate two slag mounds in Cyprus from the Late Iron Age/Classical period ($\sim$ seventh to fifth centuries BCE) and the Late Roman/Byzantine Period ($\sim$ fourth to fifth centuries CE). The aim of this study is to obtain new decadal-scale paleointensity time series of the periods represented by the Cypriot slag mounds.

2. Methods

2.1. Archaeomagnetic Sampling

2.1.1. Skouriotissa Vouppes (SU1) Slag Mound

The Skouriotissa copper mine is located near one of the major copper ore deposits in Cyprus and is the largest and longest-lived active copper mine on the island. Copper ores were extensively mined in this area through the Roman Era, leaving behind enormous slag mounds in the surrounding hills. The SU1 slag mound (35.093018°N, 32.885336°E, Figures 1 and 2) is one of the largest Late Roman/Byzantine Era slag mounds. It is located at the southern flank of the modern open pit mine and was partially exposed by road construction. The slag at SU1 is characterized by large slag pieces up to a few tens of centimeters across and up to 10 cm in thickness (supporting information Figure S1). The top part of the slag pieces is frequently glassy and exhibits vesicles and flow textures. Many of these large chunks were crushed to smaller pieces before they were dumped in the mound. Charcoal fragments ranging in size from a few mm to a few centimeters are abundant throughout the entire section (supporting information Figure S1).

Figure 2 shows a cross section of SU1. Our excavations followed an existing exposed outcrop near the road cut, here marked as "step 6." The part below step 6 was excavated to a section of laminated clay sediments that defines the base of the mound (step 7). The part above step 6 was divided to five steps $\sim$2 m in height (step 1–5). All steps were vertically leveled, cleaned, and divided into loci (archaeological layers) by visible horizons (dashed lines in Figure 2). We collected more than 400 pieces of slag, over 300 charcoal fragments, and 21 baked clay objects from the cleaned outcrops. The samples were collected from 118 different locations in 36 different loci as shown in Figure 2. The 3-D coordinates of each sampling location and loci boundaries were measured and recorded using a Total Station, allowing documentation with a spatial resolution of better than 5 cm. The total height of the studied section, as measured by the Total Station is 21.1m.

2.1.2. Mitsero Kokkinoyia (MK1)

Mound MK1 (35.042130°N, 33.106650°E, Figures 1 and 3) is located near the copper mines in the Mitsero Kokkinoyia area. Previous studies dated the activity here to the seventh to third centuries BCE, i.e., the Late

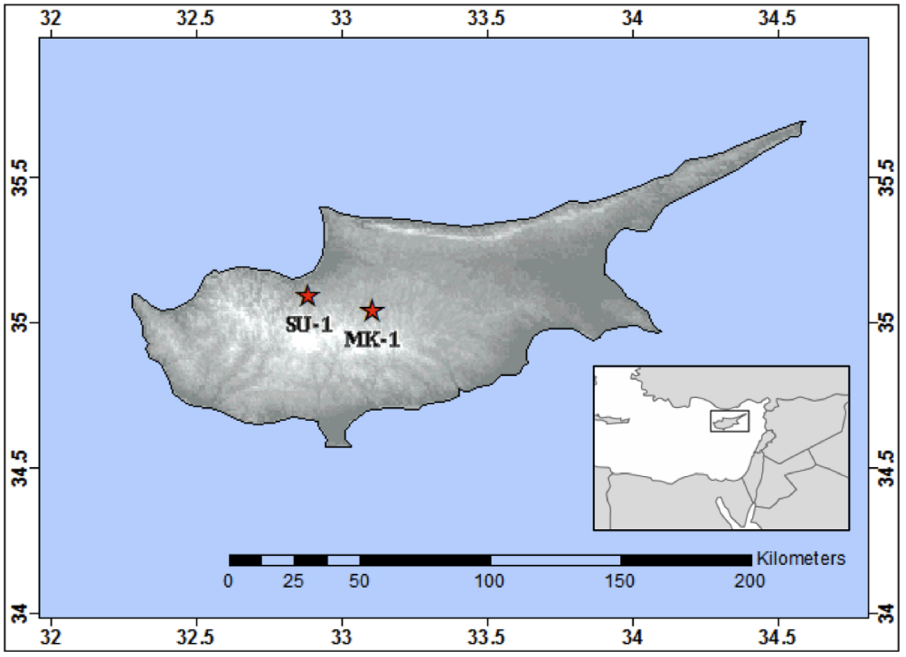

Figure 1. Location map. SU—Skouriotissa Vouppes, 35.093018°N, 32.885336°E. MK1—Mitsero Kokkinoyia, 35.042130°N, 33.106650°E.

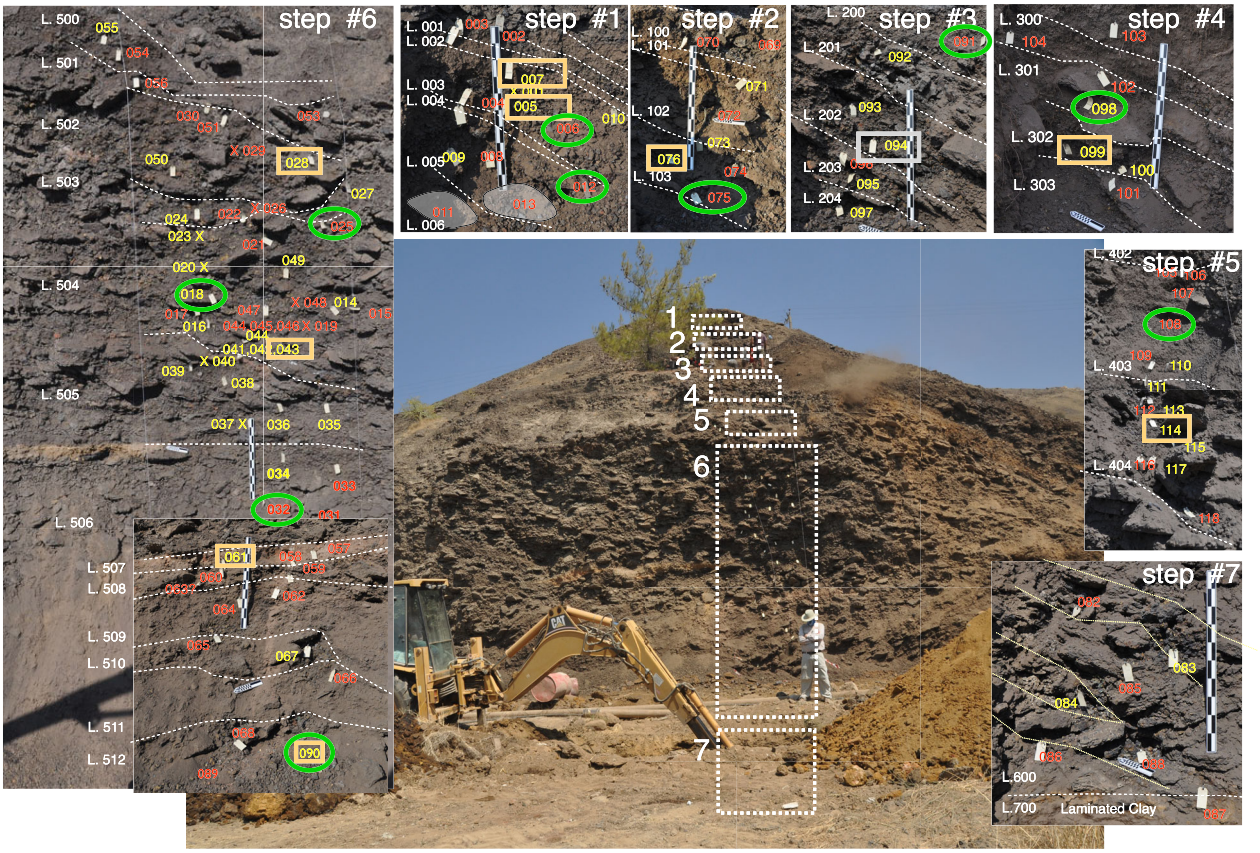

Figure 2. Slag mound SU1 (Skouriotissa Vouppes). The section is divided into seven vertically aligned "steps" and 37 loci (layers). Boundaries between loci are marked in dashed white lines and labeled with white numbers. Yellow/red numbers show the location of each sampling point in the mound. Locations with charcoal fragments are shown in yellow. Dated charcoals are marked with a frame, where gray frame marks the charcoal that was not used in the preferred age model. Slag samples that passed the selection criteria are marked in green circle.

Iron Age in Cyprus [*Kassianidou*, 2004]. The section is 8 m in height and contains a complicated sequence of slag layers separated by soil layers. Several unconformities near Loci 15, 25, 27, and 32 (Figure 3) suggest a complex history of accumulation. More than 200 pieces of slag and over 60 charcoal fragments were collected from 101 sampling locations. Nine soil layers were sampled for charcoal flotation analysis (Loci 5, 8, 12, 14, 15, 21, 23, 27, 32). Sampling locations and loci boundaries were recorded using a Total Station.

2.2. Wood Identification and Radiocarbon Dating

Wood identification of the charcoal was done at the Cornell Tree-Ring Laboratory at Cornell University. Each charcoal section was fractured with a razor blade to create fresh transverse, radial, and tangential planes [following *Cartwright and Parkington*, 1997]. The samples were examined under an Olympus Bx41 binocular microscope and Motic K-400P stereo microscope at magnifications up to x500. The characteristic features of the wood were documented, photographed, and then compared with archaeological and modern wood reference collections, standard reference texts [*Fahn et al*., 1986; *Schweingruber*, 1990; *Akkemik and Yaman*, 2012], and the InsideWood anatomical database (http://insidewood.lib.ncsu.edu/). In some cases, it was possible to identify samples only to the family or genus level, because of either physical changes to the cellular morphology from the charring process or indistinguishable anatomical features among species in the same genus or subgenus.

Nineteen charcoal samples—eleven from SU1 and eight from MK1—were selected for radiocarbon dating. Seventeen of these samples are pine (*Pinus* sp.) and are most likely *Pinus brutia* Ten. One of the samples is an evergreen oak (*Quercus* section *Ilex*). Since the mounds did not contain clearly short-lived material (like seeds), the outer rings of branch and twig samples with bark were extracted when possible for the radiocarbon analysis to minimize old wood bias [e.g., *Levy et al*., 2008]. AMS radiocarbon measurements were done at the NSF Arizona AMS laboratory, University of Arizona. Dates were calibrated and modeled with OxCal v.4.2.3 [*Bronk Ramsey*, 2009] using the IntCal13 calibration curve [*Reimer et al*., 2013].

2.3. Paleointensity Experiments

Paleointensity experiments were carried out at the paleomagnetic laboratory of Scripps Institution of Oceanography (SIO), University of California San Diego. Specimens were prepared by cutting chips of 1–5 mm in size from the glassy part of the slag. The chips were wrapped in glass filter paper and glued inside 12 mm diameter glass vials using potassium-silicate glue (KASIL). The experimental procedure followed the IZZI protocol of *Tauxe and Staudigel* [2004] with routine pTRM checks [*Coe et al*., 1978] at every second temperature step. The oven field was set to 40 or 60 μT. In total, 673 specimens from 153 samples were analyzed.

Remanence anisotropy tensors were calculated using thermoremanent magnetizations or anhysteretic remanent magnetizations (ATRM and AARM, respectively). The ATRM procedure included eight heating steps carried out at the highest temperature that the specimens reached during the Thellier experiment: a baseline step in a zero field (subtracted from the subsequent infield measurements), six infield steps in 60 μT at orthogonal directions (+x, +y, +z, -x, -y, -z), and an additional infield alteration check at the end of the experiment. AARM was done in 9 of the 15 positions in the scheme of *Jelinek* [1978, see also *Tauxe*, 2010] using 180 mT AC field and 100 μT DC field. Before each ARM step, the specimen was AF demagnetized at 180 mT and this baseline magnetization was measured and subtracted from the subsequent infield ARM measurement. Anisotropy tensors were calculated using the method of *Hext* (1963, see also *Tauxe*, 2010] via PmagPy software (http://earthref.org/PmagPy/cookbook).

Nonlinear TRM [NLT, *Selkin et al*., 2007] was checked on 167 specimens using 4–5 infield steps carried out at the highest temperature of the Thellier experiment in oven fields ranging from 20 to 80 μT. The results demonstrated that the NLT effect is insignificant (see section 3.2), and therefore, the rest of the specimens were not subjected to the NLT procedure.

The effect of cooling rate effect was tested on four specimens from the only baked clay sample in this study (su102501a). The cooling rate experiment included four steps in 590C: zero-field step (for baseline measurement), infield step at 60 mT in regular (fast) cooling rate (supporting information Figure S2), infield step at 60 mT in a slow cooling rate (supporting information Figure S2), and infield step at regular cooling rate (alteration check). Cooling rare correction (supporting information Figures S3 and S4) was calculated assuming the relation between TRM and cooling rate given in *Halgedahl et al*. [1980], assuming an averaged

ancient cooling rate of 6 h from 500 to 200°C. As slag is rapidly cooled, no cooling rate is necessary on the rest of the specimens [*Shaar et al*., 2010].

2.4. Paleointensity Data Analyses and Interpretation Procedures

The conventional technique for interpreting paleointensity data is to manually pick temperature bounds for each specimen separately. The selected temperature bound is somewhat arbitrary and reflects some subjective consideration for what is assumed to be the most appropriate temperature interval. The quality of the interpretation in commonly quantified by paleointensity statistics [e.g., *Paterson et al*., 2014] that assess different aspects of the experimental behavior. Paleointensity statistics are often used as selection criteria by assigning threshold values to each statistic. As specimen interpretations alone are insufficient to account for all sources of uncertainty, the final paleointensity estimate is usually calculated as a sample (cooling unit) mean or as a site (collection of samples of the same age) mean. The standard deviation of the mean is usually reported as the error bounds of the paleointensity estimate.

Despite the known benefits of the conventional approach for paleointensity interpretation, it has some important drawbacks. One root problem is that there is no consensus on which selection criteria and which threshold values should be used in order to screen out unreliable interpretations. This problem applies to both the specimen level (e.g., "Which statistics and what threshold values to use?," [*Paterson et al*., 2014]) and to the sample/site level ("How many specimens should be averaged?" and "How to account for internal consistency?," [*Paterson et al*., 2010]). Given the complexity of the raw experimental data, the differences between the interpretations made using different acceptance criteria may be significantly large. Another key problem is that the reported error estimation of the sample/site mean (in the form of one standard deviation) does not account for all sources of uncertainty at the specimen level interpretation.

In this work, we employ a different technique for interpreting the data. We apply the automatic interpretation available via the Pmagy Thellier-Gui (described in detail in *Shaar and Tauxe* [2013]). The main features of the automatic interpretation technique are the ability to guarantee consistency, objectivity, and reproducibility of the interpretations.

To use the automatic interpretation technique (called hereafter *STDEV-OPT*, i.e., "standard deviation optimization"), the user first has to choose acceptance criteria (from the list given in *Paterson et al*. [2014]; http://www.paleomag.net/SPD/). Then the program performs the following tasks:

1. Arai plots line fitting: the program analyzes all the possible best-fit lines of each Arai plot separately and isolates the interpretations that pass the specimen selection criteria.

2. Specimen corrections: each interpretation is corrected for the effect of anisotropy, cooling rate (for slow-cooled samples such as pottery), and if needed, nonlinear-TRM (NLT) (e.g., supporting information Figures S3 and S4).

3. Sample/site means: the program calculates all the possible sample/site means and isolates all the means that pass the sample/site acceptance criteria.

4. STDEV-OPT sample/site mean: from all the sample/site means that pass criteria, the STDEV-OPT mean ("most likely") is the one that has the lowest standard deviation (best agreement within a cooling unit or site). The uncertainty bound is the standard deviation.

5. Error bounds: the "extended" uncertainty bounds of the sample/site paleointensity are calculated by finding from all the means that passed the criteria two end-case interpretations: the lowest ($B_{min} - \sigma_{min}$) and the highest ($B_{max} + \sigma_{max}$). The "extended" uncertainty bounds are [$B_{min} - \sigma_{min}$, $B_{max} + \sigma_{max}$]. This "extended" error envelope is significantly larger than what is conventionally reported as uncertainty (1s). Nevertheless, we believe that this calculation is more robust and consistent than the conventional approach because it takes into consideration all the possible interpretation at the specimen level that pass the criteria, and not just a collection of subjective interpretations chosen by the analyst.

All the measurement data and the software to analyze it (PmagPy ThellierGui) are accessible from the MagIC database (http://earthref.org/MAGIC/) and from the PmagPy homepage (http://earthref.org/PmagPy/cookbook/), respectively. This gives other researchers full access to the raw data, and allows others to reproduce our final interpretations and reinterpret them using any given set of acceptance criteria, if they so choose.

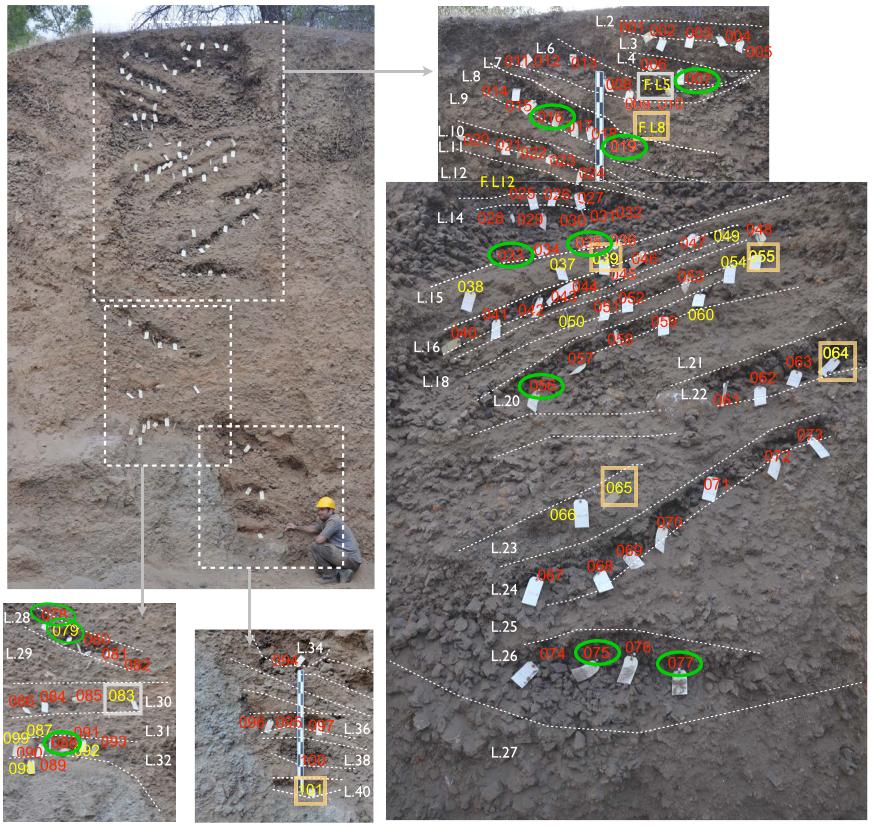

Figure 3. Slag-mound MK1 (Mitsero Kokkinoyia). Color scheme and numbering is as in Figure 2.

2.4.1. Specimen Paleointensity Statistics

The success of the automatic interpretation procedure depends on the assumption that the acceptance criteria successfully screen out unreliable interpretations. The set of statistics we use follows *Shaar and Tauxe* [2013] who argue that the use of seven statistics, as listed below, covers the most common causes for failure of a paleointensity experiment (for a detailed definition of the statistics see http://www.paleomag.net/SPD/)[*Paterson et al.*, 2014].

Figure 4a shows nearly ideal experimental results with a straight-line Arai plot [*Nagata et al.*, 1963], successful pTRM checks, and a straight Zijderveld plot [*Zijderveld*, 1967] converging to the origin. In this case, different choices of temperature bounds would yield nearly identical slopes resulting in the same paleointensity estimates. Clearly, interpretations based on such data should pass the selection criteria. Figures 4b–4f show examples of lower quality of Arai/Zijderveld plots rejected by our selection criteria. In these cases, different choices of temperature bounds yield significantly different slopes, and choosing the most appropriate slope is somewhat arbitrary. Moreover, it is clear that these specimens do not fulfill the basic assumption underlying the Thellier method (pure TRM carried exclusively by no interacting single domains that do not alter during the experiment) and thus the reliability of these interpretations is questionable.

The specimen criteria we use are as follows:

1. *FRAC* [*Shaar and Tauxe*, 2013] ≥ 0.79. FRAC is a remanence fraction statistic calculated by the vector difference sum (*VDS*) [*Tauxe and Staudigel*, 2004] of the selected component divided by the total *VDS*. A low *FRAC* indicates that only a small fraction of the remanence is used for paleointensity estimation (e.g. Figure 4b). FRAC is more suitable for general use than *f* [*Coe et al.*, 1978] and f_{vds} [*Tauxe and Staudigel*, 2004], as *f* and f_{vds} might lead to misleading high or low values, respectively, for some nonideal Arai plots (e.g., Figure 2 in *Shaar and Tauxe* [2013]; Figure 4b).

2. β [*Coe et al.*, 1978; *Selkin and Tauxe*, 2000] ≤ 0.1. β is the standard error of the least squares line slope of the selected segment in the Arai plot divided by the slope. A high β value indicates a nonlinear or highly scattered Arai plot (but low β does not always guarantee a straight line, e.g. Figure 4c).

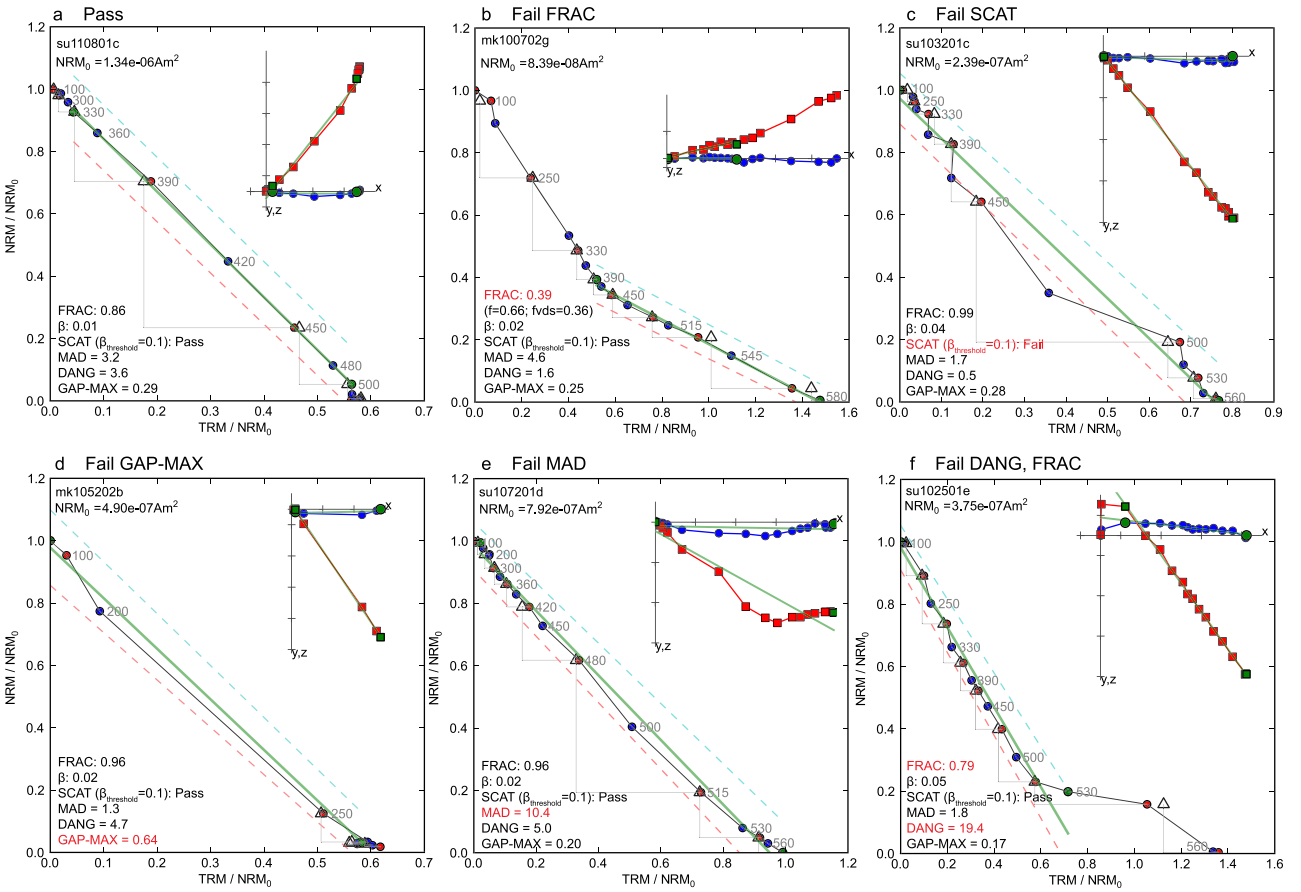

Figure 4. Examples for different behaviors in the IZZI Thellier-type experiments demonstrating our choice for the selection criteria. Red circles, blue circles, and triangles in the Arai plots are ZI steps, IZ steps, and pTRM checks, respectively. Blue (red) squares in the Zijderveld plots (insets) are *x-y* (*x-z*) projections of the NRMs in specimen coordinate system, where *x* axis is rotated to the direction of the NRM. Best-fit lines and temperature bounds are marked in green. Specimen paleointensity statistics are listed in the bottom left corner of the subplots and marked with red if failing our acceptance criteria (section 2.4). (a) Ideal behavior passing all criteria. (b) Bilinear Arai plot resulting with low fraction statistic (*FRAC*) for each linear segment. (c) Scattered and zigzaggy plot resulting in high scatter statistic (*SCAT*). Note the misleading low value of β. (d) Large gap between points in the Arai plot resulting in high *GAP-MAX* statistic. (e) High *MAD* due to nonlinear Zijderveld plot, perhaps due to displacement while cooling. (f) High *DANG* due to Ziderveld plot not converging to the origin. For more details on the selection criteria, see section 2.4.

3. *SCAT* [*Shaar and Tauxe*, 2013]: a Boolean scatter statistic relying on β. *SCAT* is determined by a polygon (dashed lines in Figure 4) drawn on the Arai plot using the threshold value of β. *SCAT* is True (pass) only if all the data points including the pTRM checks fall inside the polygon. A False (fail) value can result from nonreproducible pTRM checks, zigzagged, scattered, or nonlinear Arai plot, or a poorly defined best-fit line (e.g. Figure 4c).

4. $N_{pTRM} \geq 2$: the number of pTRM checks carried out before reaching the highest temperature in the selected segment. Fewer checks indicate that alteration was not properly tested.

5. *GAP-MAX* [*Shaar and Tauxe*, 2013] ≥ 0.5: maximum Gap Statistic. The longest vector difference between consecutive data points in the selected segment of the Arai plot, normalized by the VDS of the selected segment. A high *GAP-MAX* indicates a poorly defined Arai plot with two data points separated by a large gap (e.g. Figure 4d).

6. *MAD* [*Kirschvink*, 1980] ≤ 5: free floating maximum Angular Deviation of the principle component best fit line of the Zijderveld plot. A high *MAD* indicates a nonlinear or scattered Zijderveld plot (e.g. Figure 4e).

7. *DANG* [*Tauxe and Staudigel*, 2004] ≤ 10: the deviation angle of the Zijderveld best-fit line from the origin. A high value indicates that the Zijderveld plot does not converge to the origin (e.g., Figure 4f).

In addition to the above, alteration during the ATRM and NLT procedures is calculated by comparing the first and the last measurements. Alteration is calculated in the ATRM procedure by comparing the following

three pairs of measurements (after baseline subtraction): +x and −x, +y and −y, +z and –z. The threshold value for the alteration check is 5%.

2.4.2. Sample Paleointensity Statistics

At the sample level (sample = cooling rate unit), we use the following statistics as acceptance criteria:

1. $N_{sample} \geq 3$: minimum specimens required for samples mean calculation.

2. $\sigma\ (\mu T) \leq 3\ \mu$T: standard deviation of the sample mean (absolute value).

3. $\sigma\ (\%) \leq 8$ %: standard deviation of the sample mean divided by the mean in units of %.

The last two statistics are combined with a logical "or" function, i.e., σ passes the criteria if $\sigma \leq 3\ \mu$T or $\sigma\ (\%) \leq 8$ %.

In addition, specimens that failed the anisotropy procedure (e.g., due to alteration), and specimens that were not corrected for anisotropy because specimens fell apart from the glass tube, were excluded from sample mean calculation.

2.5. Hysteresis and FORCs

To better understand the rock magnetic characteristics of the slag material, we measured hysteresis loops of one specimen from each sample that passed the final acceptance criteria. In addition, we collected first-order reversal curves (FORC) [*Pike et al*., 1999] from six specimens—three from each mound. Hysteresis and FORCs were collected using a Princeton Measurements Vibrating Sample Magnetometer (μVSM) at the Institute of Rock Magnetism (*IRM*), University of Minnesota. Hysteresis data were analyzed via PmagPy software package [*Tauxe*, 2010]. FORCs were analyzed using FORCinel software [*Harrison and Feinberg*, 2008].

2.6. Electron Microscopy

To identify the ferromagnetic phase carrying the ancient TRM, electron microscopy was used to examine selected slag specimens that passed the acceptance criteria. Specimens were embedded within phenolic resin and polished to 25 nm using colloidal silica for scanning electron microscope imaging and elemental analyses. Crystallographic information on the silicate and oxide mineralogy within the slag samples was obtained from polished sections using a JEOL 6500 field emission gun (FEG-SEM) outfitted with an HKL electron backscatter diffraction (EBSD) detector at the University of Minnesota. EBSD measurements were conducted using an operating voltage of 20 kV and a working distance of 25 mm. Minerals were identified by indexing diffraction patterns using Channel 5 software. Crystallographic solutions were accepted only if the mean angular deviation (MAD) value was less than 1.4°. Measurements of elemental abundances were collected using an accelerating voltage of 15 kV and a working distance of 10.0 mm. Spot energy dispersive spectroscopy (EDS) measurements were collected using a Thermo-Noran Vantage System. The diameter of the interaction volume for elemental measurements was ~2.5 μm in silicate minerals and ~2.0 μm in oxide and sulfide minerals. Matrix correction coefficients (Z, A, and F) were calculated using the Phi(Rho*z) method of *Pouchou and Pichoir* [1984] and *Bastin and Heijligers* [1991]. X-ray spectra were collected using counting times of 60 s and a probe current of 100 nA.

3. Results

3.1. Radiocarbon Results and Age-Height Models

Chronological models of the mounds were constructed using Bayesian analysis, which combines *prior* information (stratigraphic order of the samples and their relative heights) with standard *likelihood* information (absolute radiocarbon dates). The analysis is done via the Oxcal program [*Bronk Ramsey*, 2009]. The Oxcal input programs, the radiocarbon dates, and the Oxcal output table are listed in an Excel file in supporting information.

3.1.1. SU1

The prior information in SU1 is the relative heights of the samples measured by the Total Station. As we do not have any prior information on the deposition rate, we assume random changes in deposition rate. This is done using the P_Sequence procedure in Oxcal [*Ramsey*, 2008]. In addition, as we do not know the increments of the chronological pieces, we follow *Bronk Ramsey and Lee* [2013] and simulate different age-depth models using a range of increments from 1 mm to 1 m. The final age-height model is the average of all the simulated models. To test the Poisson height-depth model, we ran a "Sequence" model that uses the stratigraphic order of the samples as priors and ignores their heights. The Sequence model is more flexible than

the P_Sequence model, but it cannot be used to model the height-age relation. The results of the Sequence P_Sequence models are nearly identical.

An initial P_Sequence analysis of the calibrated radiocarbon ages of SU1 shows that in general, the sample age increases with depth, such that the oldest samples are at the bottom of the mound. Some shifts from the general age-depth trend are seen, but these are expected because of specific uncertainties in the chronological analysis that cannot be completely eliminated, such as the time gap between the age of the stem when it was cut and the time when it was used and dumped in the mound (the "Old Wood Effect", important especially when the outermost ring is unidentifiable). The agreement index (the overlap of the posterior probability and the likelihood probability distributions) of the initial P_sequence model is lower than is normally considered acceptable $A_{model} = 40\% < 60$ % due to an exceptionally low agreement index (3.1%) of sample su1094. If we discard the outlier sample su1094, we get $A_{model} = 146$ and sample agreement indices well above acceptable values. The age model discarding sample su1094 is shown in Figure 5b.

The P_sequence procedure yields a height-age model with likelihood probability distributions for each height in the mound. The height-age model is used to assign an age distribution for each of the slag samples. The age constraints for the bottom and the top of the mound are: (1) bottom: 68.2% probability range = 362 to 404 CE, 95.4% probability range = 321 to 416 CE, median=380, (2) top: 68.2% probability range = 403 to 440 CE, 95.4% probability range = 397 to 531 CE, median=426. These distributions suggest that the mound was accumulated in a period of about 46 years (difference between the medians), with 68.2% probability range of 78 years, and 95.4% probability range of 210 years.

3.1.2. MK1

There are three main difficulties in dating the MK1 mound. (1) Identifying the wood species and isolating the outermost rings was difficult because the charcoal is poorly preserved, consisting of mostly small fragments, and there are fewer samples with preserved bark and/or outer rings. (2) The dates are located within the so-called "Iron Age plateau" in the ^{14}C calibration curve (supporting information Figure S5), resulting in a large dating uncertainty. (3) There is no consistent age-height correlation between the ^{14}C age and stratigraphic level throughout the mound (unlike in SU1, see Figure 5). Therefore, we model the ^{14}C dates in MK1 as a single Phase in OxCal program. This model does not assume any correlation between charcoal age and depth.

Figure 5c shows the likelihood functions of the calibrated ages from MK1 ordered according to their stratigraphic position in the mound. We recall that the quality of the charcoals from MK1 is significantly lower than in SU1. The ages of six samples overlap and their ages range from the eighth to the beginning of the fourth centuries BCE. Two other samples have ages that differ from the unmodeled date ranges: charcoal fragment mk1L.5, which was sampled from flotation and has an older age range, and sample mk1083, which is younger than the other samples. It is possible that there is some mixing of fine materials within the mound, which might introduce younger material (like mk1083) into an older context (or vice versa). Small charcoal fragments (like mk1L.5, which is only 1 mm) can be especially mobile. It is also possible that mk1L.5 is older because of old wood bias, since it is not known if the sample is part of the outermost part of a branch/twig.

In MK1, we do not use the stratigraphic order of the radiocarbon dates in the age modeling. Instead, we group all the eight samples as one phase. The supplemental Excel file lists Oxcal output for three different models. "Model 1" uses all the ages, "Model 2" discards sample mk1083, and "Model 3" discards samples mk1083 and mk1L.5. "Model 3" is our preferred model as it excludes dates that are likely unreliable. We use the resulting age model to assign an age to each layer (locus) by evenly distributing the difference between the modeled likelihood distributions of the top and the bottom of the mound among the slag layers. This age model assumes a constant deposition rate, and helps put the paleointensity results in a chronological reference frame. However, we note the large uncertainty in this age model.

3.2. Paleointensity

The strict specimen acceptance criteria listed in section 2.4 were chosen to screen out unreliable behavior in the paleointensity experiments exemplified by nonlinear Arai plots, unreproducible pTRM checks, curved or diverging Zijderveld plots, and poorly determined anisotropy tensors. A total of 267 specimens (out of

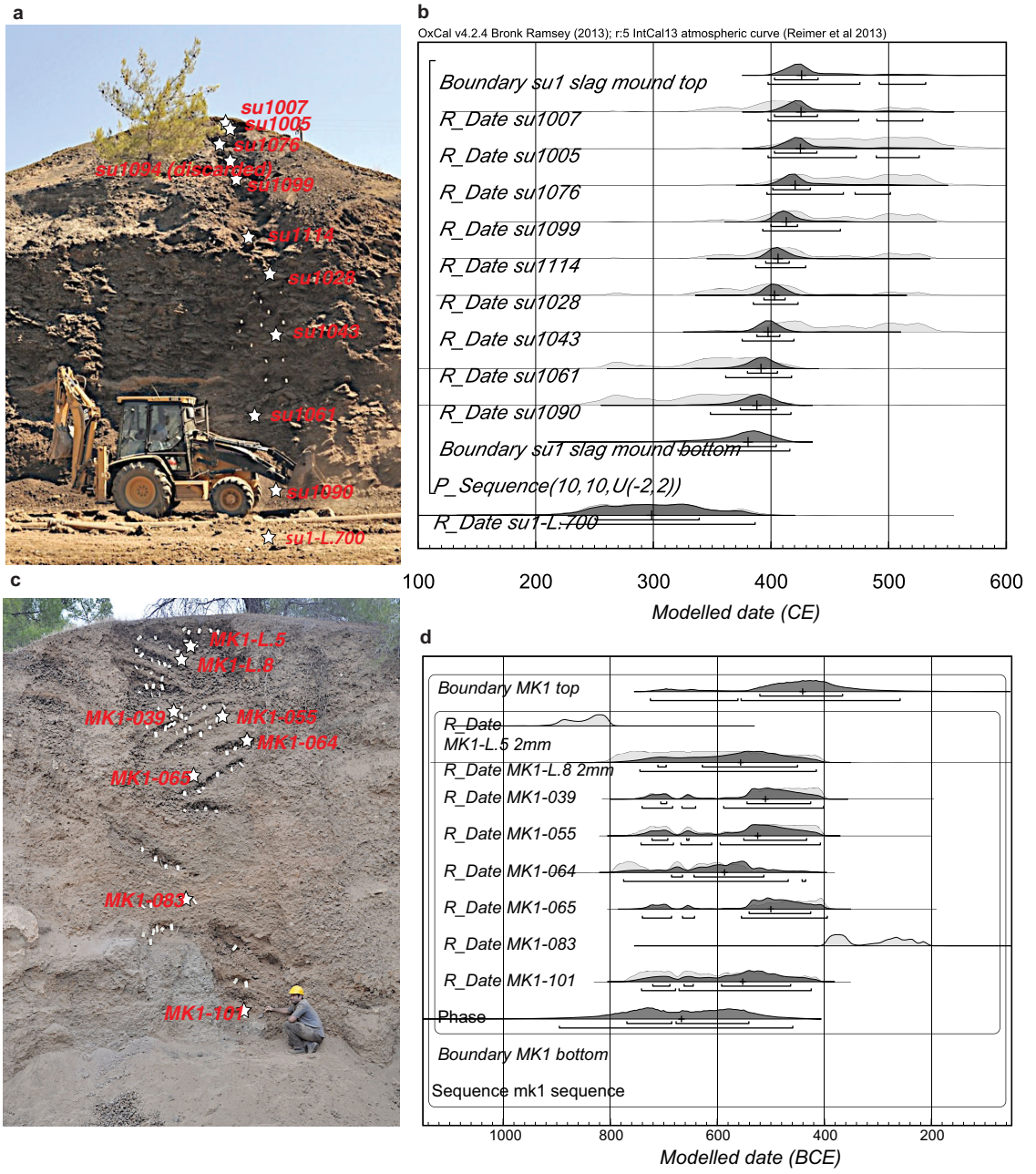

Figure 5. Radiocarbon data. Stars on the cross sections (a,c) show the location of radiocarbon samples. The exact locations are also shown in Figures 2 and 3, and the measured stratigraphic height is given in supporting information excel file. (b,d) Radiocarbon likelihood distributions of the calibrated ages are shown in pale gray. Likelihood distributions of the Bayesian modeled ages (section 3.1) are shown in dark gray. Brackets and crosses represent the 68.2% and the 95.4% probability ranges and the medians. Figure was produced using OxCal v.4.2 program [*Bronk Ramsey*, 2009]. For more information see supporting information.

673) passed specimen acceptance criteria. This low, but reasonable rate of success (40%) reflects the difficulty in isolating specimens with high quality behavior such as in Figure 4a. Supporting information Figure S6 displays a histogram showing the distribution of the anisotropy degree ($P=\tau1/\tau2$) of the specimens that passed the selection criteria, demonstrating that most of the specimens exhibit relatively high P values. For this reason, we discard specimens that failed the anisotropy experimental procedures from sample mean calculations (e.g., alteration observed during the ATRM procedure, or because the glue holding the specimen in the vial got loose during the anisotropy experiment at high temperature). Supporting information Figure S6 shows histograms of the NLT correction. Except for a few cases, the NLT correction was less than 4% suggesting that NLT effect is insignificant.

Table 1. Sample Paleointensity

Sample	Mound	Locus or Height[a]	Age Model[b] Median	68.2% Low	68.2% High	n	Optimal σ(STDEV-OPT)[c] B $\pm \sigma$	VADM $\pm \sigma$	Extended Error Envelope[d] B (μT)	VADM (ZAm^2)
mk100702	mk1	4	−465	−545	−391	8	60.3 ± 4.7	110.5 ± 8.6	55.6 − 65.0	101.9 − 119.1
mk101601		8	−489	−569	−415	6	75.1 ± 1.9	137.8 ± 3.5	68.0 − 81.6	124.7 − 149.7
mk101901		8	−489	−569	−415	4	70.0 ± 4.1	128.3 ± 7.5	63.5 − 75.9	116.5 − 139.2
mk103302		14	−537	−617	−463	4	67.4 ± 4.7	123.5 ± 8.6	62.7 − 72.0	114.9 − 132.1
mk103501		14	−537	−617	−463	5	73.2 ± 5.8	134.2 ± 10.7	67.4 − 79.0	123.5 − 144.9
mk105601		20	−573	−653	−499	4	69.7 ± 2.8	127.8 ± 5.2	61.4 − 77.2	112.6 − 141.5
mk107501		26	−621	−701	−547	4	73.0 ± 4.1	133.9 ± 7.5	65.8 − 81.5	120.6 − 149.5
mk107701		26	−621	−701	−547	6	71.8 ± 5.6	131.6 ± 10.2	66.2 − 77.4	121.4 − 141.8
mk107801		28	−633	−713	−559	6	75.2 ± 5.5	137.8 ± 10.0	69.7 − 80.6	127.7 − 147.8
mk107901		28	−633	−713	−559	5	72.0 ± 4.5	132.1 ± 8.3	66.0 − 80.5	120.9 − 147.5
mk107902		28	−633	−713	−559	4	69.5 ± 3.3	127.4 ± 6.0	64.7 − 75.1	118.7 − 137.7
mk108801		32	−657	−737	−583	8	73.9 ± 3.2	135.5 ± 5.9	68.1 − 81.5	124.8 − 149.5
su109001	su1	3.63	388	374	404	8	60.0 ± 2.4	110.0 ± 4.4	52.5 − 66.2	96.2 − 121.4
su103201		6.03	393	382	406	5	53.4 ± 3.1	97.9 ± 5.6	47.9 − 57.4	87.8 − 105.3
su101801		8.34	399	390	409	8	66.1 ± 2.4	121.1 ± 4.3	58.0 − 71.9	106.2 − 131.8
su102501[e]		9.16	401	392	411	4	57.8 ± 0.1	105.9 ± 0.1	54.1 − 67.5	99.1 − 123.7
su110801		12.37	408	397	418	7	67.0 ± 2.9	122.8 ± 5.4	59.4 − 73.6	108.9 − 134.8
su109801		15.02	413	400	423	3	61.9 ± 4.2	113.5 ± 7.7	57.1–67.3	104.6 − 123.3
su109102		18.08	419	401	431	5	57.7 ± 2.2	105.7 ± 4.1	53.6 − 61.6	98.3 − 112.9
su107501		18.69	420	401	433	7	56.7 ± 3.1	103.9 ± 5.6	49.8 − 64.1	91.2–117.5
su101201		20.83	424	402	438	3	50.9 ± 0.4	93.2 ± 0.7	46.4 − 59.6	85.0 − 109.1
su100601		21.15	424	403	438	4	44.1 ± 0.9	80.8 ± 1.7	42.7 − 46.6	78.3 − 85.4

[a]Locus number refers to the layer numbering of MK1 in Figure 3. Height is the relative elevation of the samples in SU1 mound.
[b]See section 3.1 and supporting information for age models.
[c]STDEV-OPT is the algorithm in the Thellier GUI program [*Shaar and Tauxe*, 2013] that choose from all the acceptable means that pass the acceptance criteria the mean with the minimum σ%. All results are corrected for anisotropy (and NLT if needed). See section 2.4 for details.
[d]Minimum and maximum possible means that pass the acceptance criteria ± their standard deviation.
[e]Baked clay fragment (tile or furnace wall). Results are corrected for cooling rate effect (see supporting information).

With no criteria at the sample level that test the internal consistency in the cooling unit, we get 40 samples that have at least three successful specimens. Yet, the overall data exhibit significant discrepancies (supporting information Figure S9). To screen out the noisy data, we apply the criteria at the sample level ($\sigma \leq 3$ μT or $\sigma\% \leq 8$ %) and get 22 successful samples passing.

The overall low success rate (22 samples out of 153 analyzed) and the difficulty in isolating well-behaved specimens suggests that, in general, the Cypriot copper slag may not be an ideal paleomagnetic recorder. Yet, in this work, we demonstrate that with sufficient laboratory effort and strict choice of selection criteria at the specimen and sample level, a useful number of robust paleointensity estimates can be obtained.

Table 1 lists the final paleointensity estimates of the samples. The STDEV-OPT mean is the mean that has minimum standard deviation, the STDEV-OPT sigma is the standard deviation of the mean (the conventional estimate for error bounds in paleointensity studies), and the "extended error bound" is the maximum/minimum means that passed the criteria +/− their standard deviations (see section 2.4 for details). We treat STDEV-OPT mean as the "most likely" result as it reflects the best internal consistency within the cooling unit, but prefer the larger "extended error bound" as our error estimation. All samples are slag material except su102501 (baked clay).

Figures 6a and 6b show the paleointensity time series from SU1 plotted versus height (a) and versus age (b). Horizontal error-bars in Figure 6b show the 68.2% probability range of the modeled ages. Blue (short) *y* error bars are the standard deviation, and the red (long) error bars are the STDEV-OPT extended error bounds. The extended error bars of the SU1 data (red) are mostly overlapping. However, the SU1 data suggest an interesting steady decrease in field intensity during in upper part of the mound. This behavior is discussed in details in section 4.1.

Figure 6c show paleointensity time series from MK1 plotted versus age, where the large horizontal (age) error bars are not displayed for clarity. The data from MK1 data demonstrate excellent agreement between samples collected from the same loci, i.e., samples that are expected to yield similar paleointensity results. All the extended error bars (red), except one (sample mk100702) overlap suggesting that any changes in the geomagnetic field intensity were small and undetectable.

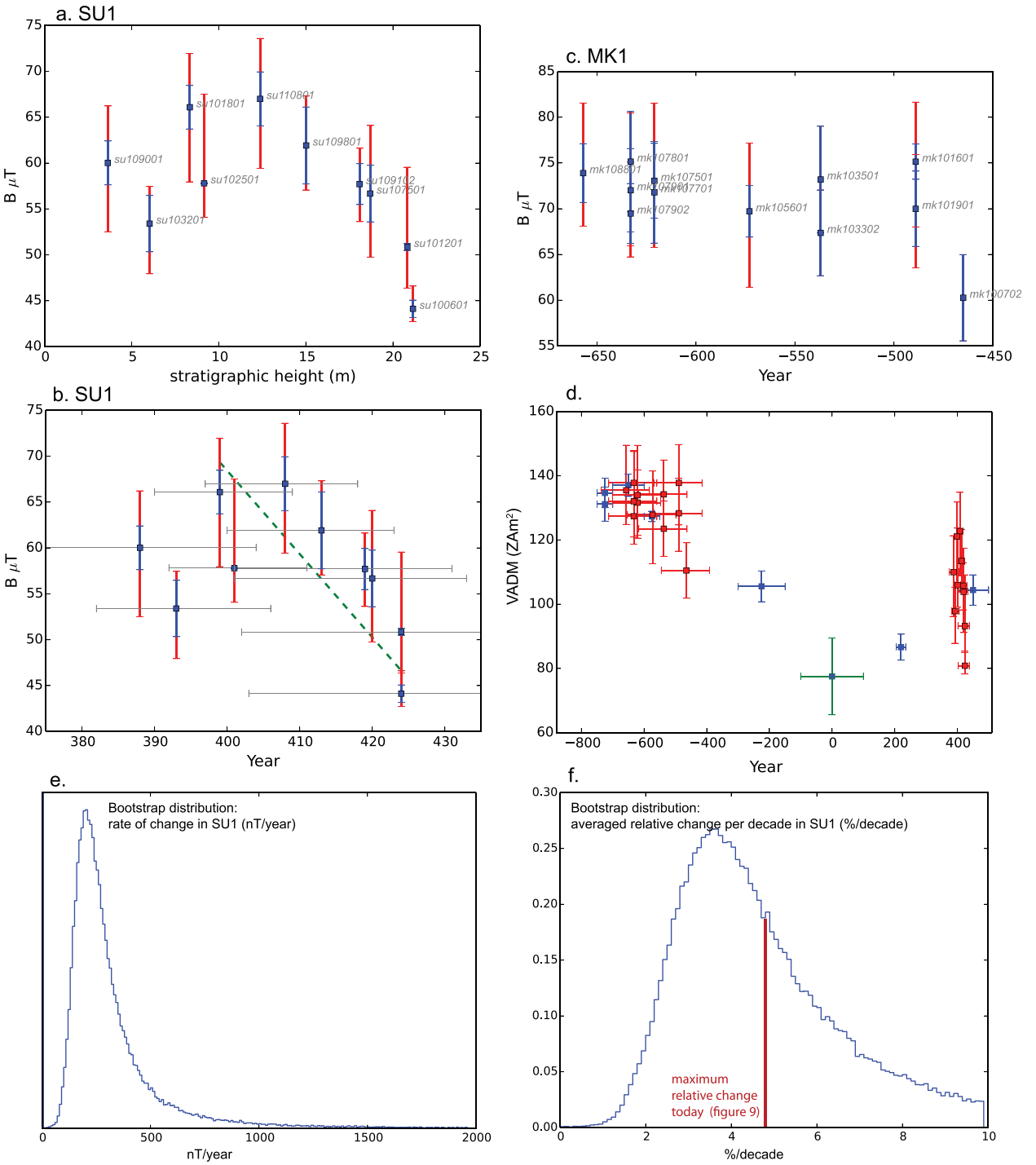

Figure 6. Paleointensity plots. (a) SU1 paleointensity displayed versus height. (b) SU1 paleointensity displayed versus modeled age. Horizontal error bars in are the 68.2% probability range of the modeled ages. Green-dashed lines show the weighted least squares line of the top eight samples. (c) MK1 paleointensity displayed versus modeled age. In (a)–(c), the blue vertical error bars are the standard deviations of the STDEV-OPT mean calculated using the automatic interpretation procedure of the Thellier-GUI (Table 1). Red error bars show the minimum and the maximum sample means that pass the acceptance criteria ± their standard deviations (see section 3.4 for details). (d) VADM estimates from previous studies: Blue symbols are *Genevey et al.* [2003] and *Gallet et al.* [2006]. Green symbol is *Ben-Yosef et al.* [2008]. (e,f) Bootstrap distributions of the rate (nT/year) and the relative % change in intensity ($100 \cdot \frac{B_{max} - B_{min}}{mean(B_{max}, B_{min})}$, where B_{min} and B_{max} are the endpoints B values) calculated using the eight uppermost samples in SU1.

Figure 6d shows the new data from this study with previously published data from Israel and Syria [*Ben-Yosef et al.*, 2008a, 2008b; *Genevey et al.*, 2003; *Gallet et al.*, 2006]. The agreement between the averaged values in MK1 and SU1 and the contemporaneous average values from Syria is excellent.

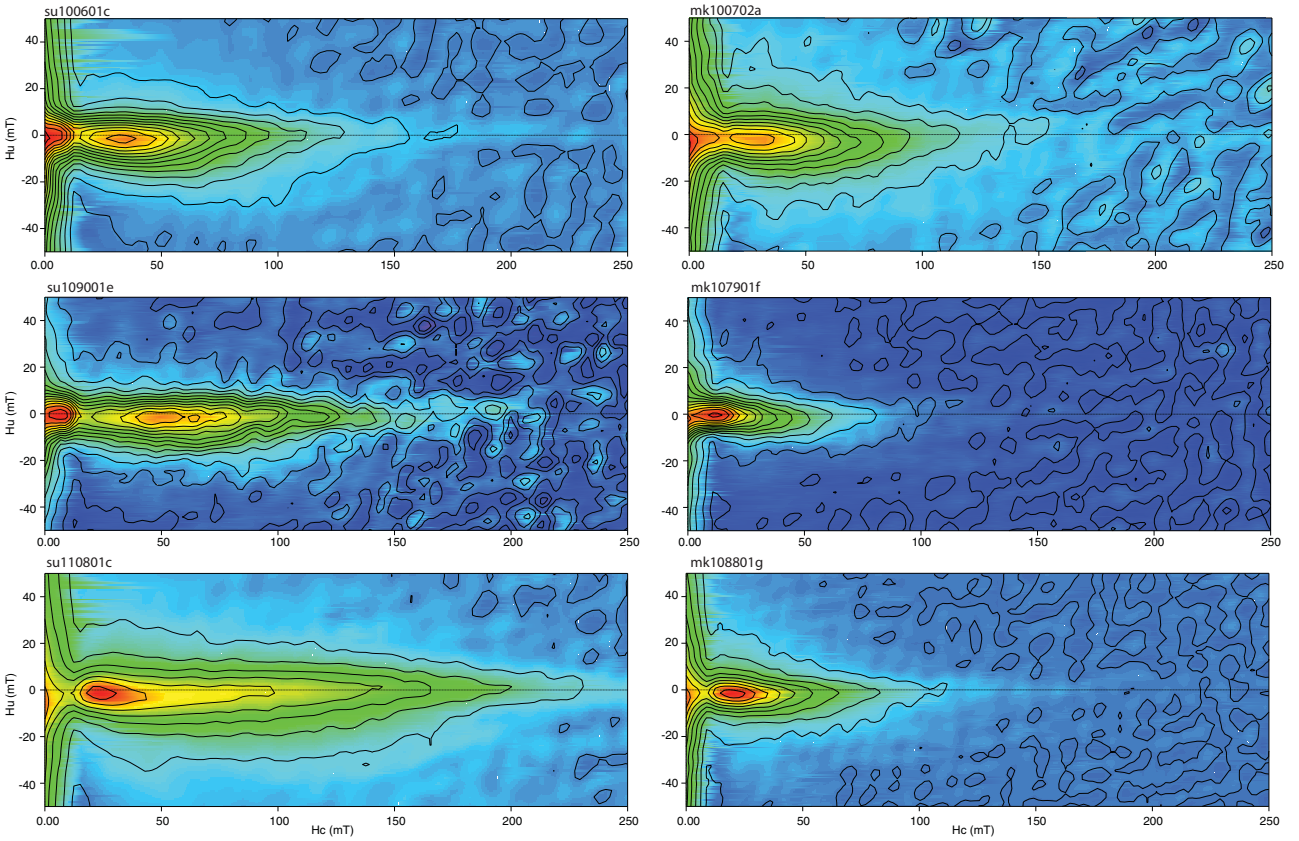

Figure 7. FORC distributions produced using FORCinel program [*Harrison and Feinberg*, 2008]. Plots use the same horizontal and vertical scale for comparison.

A MagIC Project folder that includes formatted files with the raw data, the paleointensity interpretations, and the acceptance criteria, can be downloaded from the MagIC database (http://www.earthref.org/MAGIC/).

3.3. Hysteresis and FORC

Supporting information Figure S7 show Day diagram [*Day et al.*, 1977] and squareness versus coercivity plot [*Tauxe et al.*, 2002] of the specimens that were selected for hysteresis analysis. The hysteresis parameters fall in the PSD region and may represent a mixture of different domain states [*Dunlop*, 2002]. In general, specimens from MK1 and from SU1 are grouped in different fields in the diagrams, where specimens from SU1 fall closer to the ideal SD region and have higher coercivities. The FORC diagrams shown in Figure 7 (See also supporting information Figure S8) indicate that slags from both mounds exhibit a mixture of two populations: MD, which dominates the lower coercivity spectrum ($Hc \leq 10$ mT) and small PSD to SD with symmetric interaction distributions about the $Hu = 0$ axis that extend as high as 200 mT (Figure 7c). The median values of the coercivity distributions range from 25 to 50 mT for the SU1 specimens, and from 15 to 30 mT for the MK1 specimens. The FORC analyses indicate that glassy slag material can contain a large population of high coercivity SD-like particles, which may act as ideal paleointensity recorders. Yet, as noted earlier, isolating this "SD" part of the slag while excluding the multidomain component is a challenging task with low rate of success.

3.4. Electron Microscopy

Representative SEM images of SU and MK slags are shown in Figure 8 and capture a sense of the wide variations in mineralogy, grain size and shape, and crystallization order that can occur in metallurgical slags. The general mineralogy of all of the slag samples can be divided into four categories: Cu-rich sulfide grains (sometimes rich in Fe), silicate minerals, oxide minerals, and silicate glass, where the latter phase serves as the matrix for the slag.

Cu-rich sulfide minerals, often with high concentrations of Fe, were observed in all samples in varying concentrations. Grain sizes were often smaller than the interaction volume of the electron beam, preventing

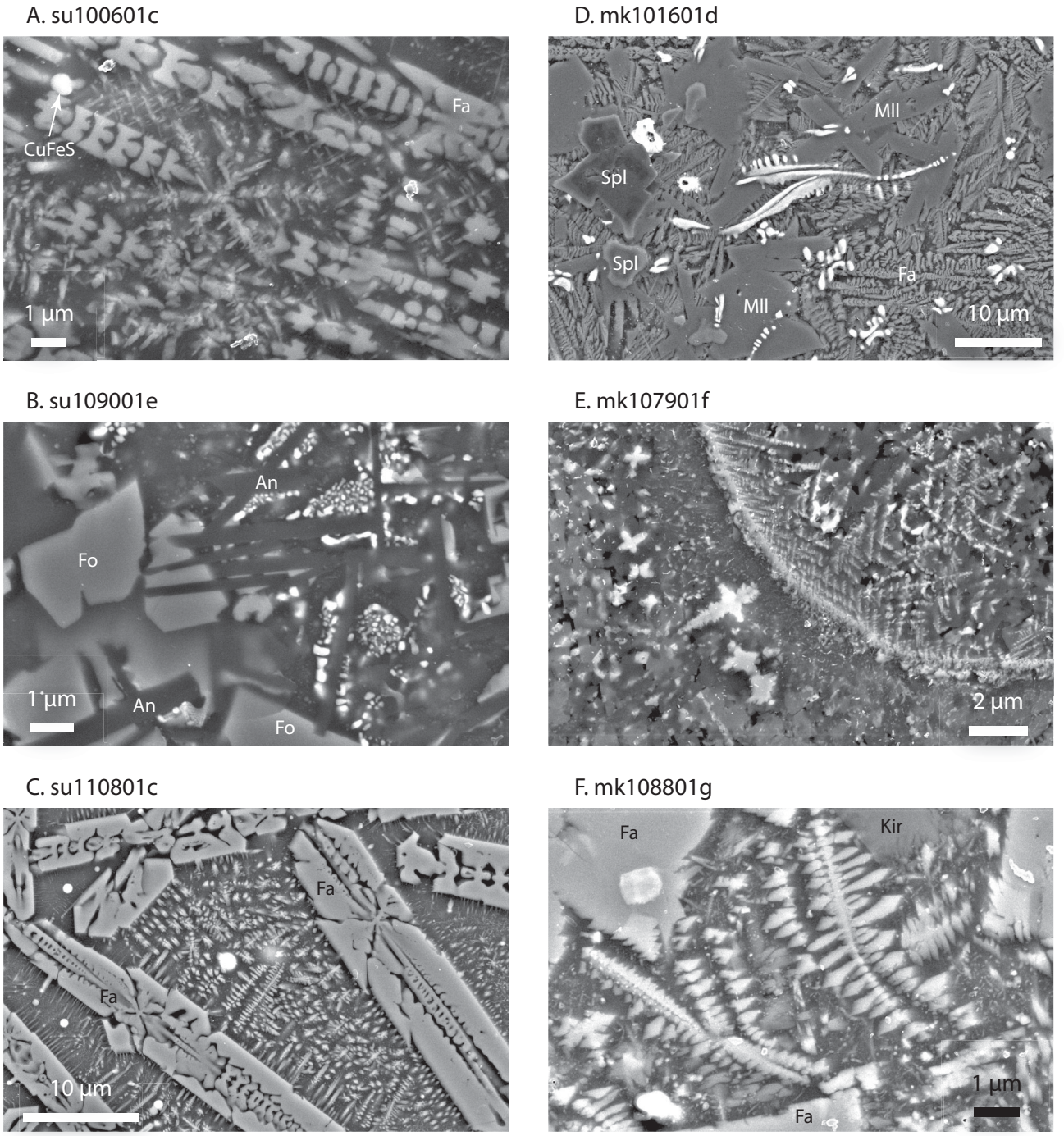

Figure 8. Representative backscattered electron micrographs of Cypriot slag. (a) Fine dendrites of magnetite growing between larger skeletal laths of fayalitic olivine (Fa). Light colored grains label (CuFeS) are iron-sulfide minerals. (b) Aggregates of submicrometer-sized grains of titanomagnetite occuring between elongated laths of anorthitic plagioclase (An). Forsteritic olivine (Fo) and CuFe-sulfide are also present. (c) Magnetite dendrites with submicrometer branches nucleating in a crystallographically controlled manner from the edges of larger, skeletal fayalitic olivine grains. Bright white grains are CuFe-sulfides. Dark gray is glass. (d) Coarse dendrites of magnetite between melilite (MII) and fine fayalite dendrites. Spinel (Spl) grains were common in this sample. (e) Magnetite dendrites nucleating at a quench surface on a fragment of preexisting slag. Coarser magnetite dendrites can be seen on the left side of the image surrounded by olivine and glass. (f) Magnetite dendrites occurring within the interstitial space between fayalite and kirschsteinite (Kir). Mineral abbreviations are from *Whitney and Evans* [2010].

unambiguous elemental measurements, although EBSD patterns indicate that sulfides with cubic, monoclinic, and hexagonal crystal symmetries are present. Grain boundaries were typically well-rounded (droplet-like) and many grains displayed internal structure suggestive of intergrowths between multiple sulfide

phases. Many Cu-Fe-S minerals are known to alter to magnetite during heating, especially between temperatures of 300 and 450°C. Such alteration can often cause paleointensity experiments to fail, as the new magnetite will cause a specimen to acquire an anomalously high remanence during pTRM steps.

The particular silicate assemblage present in a slag specimen is a reflection of the composition of the ores that were employed in smelting, the cooling rate, and oxygen fugacity of the silicate melt. As such, a diversity of silicate phases and textures were observed in specimens from SU1 and MK1. Olivine was the most frequently occurring silicate mineral, and although no end-member compositions were observed, olivine compositions ranged from fayalitic (Figures 8a, 8c–8f) to forsteritic (Figure 8b), and in one instance kirschsteinite ($CaFeSiO_4$) was observed (Figure 8f). Although there is a solid solution between fayalite and kirschsteinite, occurrences of the latter are rare in nature and are typically restricted to Ca-Fe-rich silicate melts that are silica-undersaturated and allowed to cool in low-pressure conditions. This is exactly the environment that exists for most metallurgical slags, where kirschsteinite can be common [*Wyderko and Mazanek*, 1968]. Olivine grains generally occur as large skeletal laths that confine the sizes and shapes of other minerals in the slag, an indication that they nucleated from the melt first and grew fastest (Figures 8a, 8c, 8f). Other silicates include anorthite ($CaAl_2Si_2O_8$) (Figure 8b) and melilite, $(Ca,Na)_2(Al,Mg,Fe^{2+})[(Al,Si)SiO_7]$ (Figure 8d), which occurs naturally in metamorphosed limestones, in modern industrial slags [e.g., *Broadbent*, 1987; *Min'ko et al*., 1988] as well as in archaeological slags [e.g., *Manasse and Mellini*, 2002].

Nearly pure magnetite is the most common oxide present in the slags from both SU and MK. Minor substitution of Ti, Mg, and Al may be possible in some instances, but is difficult to conclusively demonstrate owing to the extraordinarily fine scale of the dendrites relative to the interaction volume of the electron beam. Grains are usually dendritic with branches that extend for several micrometers and end as nanometer-scale branch tips. Such fine-scale dendritic structures have been shown previously to produce SD-like behavior [*Shaar and Feinberg*, 2013]. The dendrites show twofold and threefold symmetry, index as cubic, and are slightly smaller in scale in samples from the SU mound. In several instances, it is clear that the magnetite dendrites are nucleating in a crystallographically controlled manner from the edge of a nearby large silicate phenocryst (e.g., Figure 8c). This kind of topotactic growth is common in rapidly cooling systems and may provide some explanation for the exceptional remanence anisotropy observed in some samples. In the one instance, titanomagnetite occurs as aggregates of nanometer-scale grains clustered between laths of anorthitic plagioclase rather than as dendrites (Figure 8b). Fe-bearing spinel also occurs in a more limited extent in some of the MK samples.

The internal textures of the slag specimens may also provide information about why some specimens fail during paleointensity experiments. Some samples display large silicate xenocrysts, indicating that certain silicate minerals were not completely melted during the smelting process. Others showed brecciated textures infilled by silicate glass (e.g., SU-109001e). Another specimen (MK-107901f) displayed internal quenching surfaces (Figure 8e) indicating that the specimen is actually a glass agglutinate, where molten glass was deposited onto a previously cooled surface. In the case of brecciated and agglutinated slags, there is the possibility that more that one component of thermoremanence may be retained within a single specimen. Such multicomponent demagnetization curves have the potential to create large MAD values, exceeding the threshold quality control criteria, causing a paleointensity experiment to fail (e.g., Figure 4e).

4. Discussion

4.1. Decadal Rates of Change in Geomagnetic Field Intensity

The main objective of this study is to document any subcentury-scale variations in the intensity of the ancient field recorded in the Cypriot slag mounds. We investigate two slag mounds—MK1 (seventh to fifth centuries BCE) and SU1 (fourth to fifth century CE). MK1 yielded 12 reliable paleointensity means that passed our strict selection criteria (Table 1). All the samples in MK1, except one, have overlapping extended error bounds (red bars in Figure 6), and therefore, we consider them to be statistically indistinguishable. We recall that the chronology of MK1 could not be precisely estimated because of the quality of the charcoals and the "Iron Age plateau" in the ^{14}C calibration curve (section 3.1). Regardless the difficulty in establishing the exact chronology of MK1, most of the MK1 time series indicates a relatively smooth behavior of the field with no substantial changes in field intensity that could be detected by the paleointensity procedure.

In contrast to MK1, the SU1 data suggest a changing geomagnetic field. Figure 6b show an increase in field intensity until a peak value around ~ 400 – ca. 410 CE (samples su101801 to su110801) followed by a steady

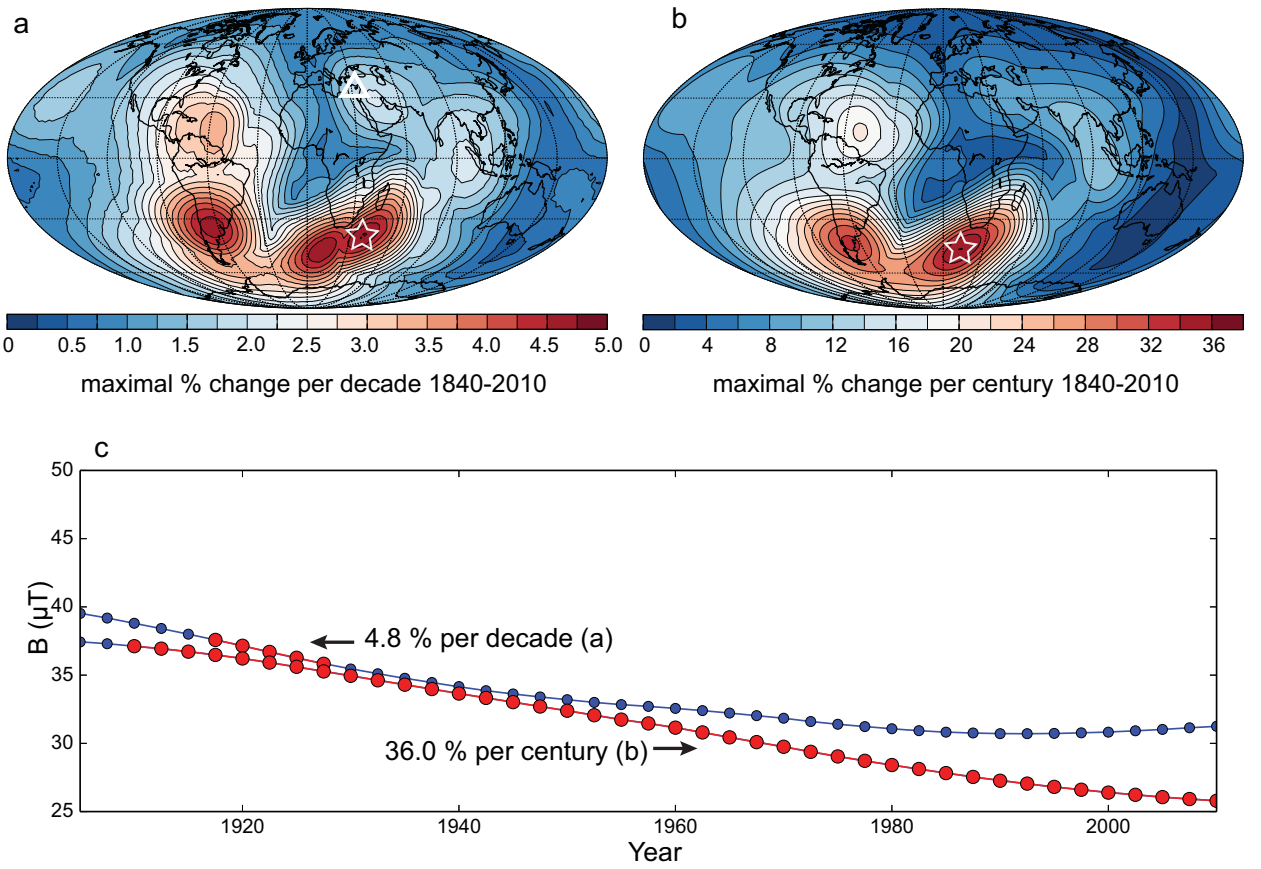

Figure 9. Maps of maximal relative rates of change in the historical field (1840–2010). The relative rates ($100 \cdot \frac{B_{max}-B_{min}}{mean(B_{max},B_{min})}$, where B_{min} and B_{max} are the endpoints B values in the selected time window—10 or 100 years) were calculated using gufm1 model [*Jackson et al.*, 2000] from 1840 to 1990 and IGRF models [*Finlay et al.*, 2010] from 1990 to 2010. (a) Maximum relative rate in a time window of 10 years. (b) Maximum relative rate in a time window of 100 years. The locations with the highest relative rates are marked with stars. Our study area is marked with triangle. The most active areas are confined to narrow lobes mostly in the southern hemisphere. Our study area is the same longitudinal band as the most active lobe near South Africa. (c) Intensity changes in the historical field (1840–2010) plotted at the location marked in stars in (a) and (b).

decrease. The slope of this line, calculated by a *y* error weighted (red error bars) least squares line over eight samples from su101801 onward is shown as a green dashed line in Figure 6b.

We try to put some constraints for the rate of the decrease shown in Figure 6b using a bootstrap analysis on eight samples from su101801 onward. In each bootstrap iteration, an *x* axis value is drawn from each sample (N-1 samples) assuming a normal age distribution (using the μ,σ of the height-age model), and a *y* axis value is drawn assuming a uniform distribution within the "extended error bounds" (the red error bars in Figure 6). As the age distribution overlap, the stratigraphic order of the samples is forced. In each bootstrap iteration, we calculate the slope of the least squares line (nT/year), and the relative change in terms of % change ($100 \cdot \frac{B_{max}-B_{min}}{mean(B_{max},B_{min})}$, where B_{min} and B_{max} are the endpoints B values at the endpoints ages of the extrapolated line). The latter calculation is done in order to be able to compare rates of changes for different absolute field intensities. The bootstrap distribution of the rate (nT/year) is shown in Figure 6e. The bootstrap distribution of the relative change per decade (%/decade) is shown in Figure 6f.

4.2. Comparison With the Historically Measured Geomagnetic Field

The data from the Cypriot slag mound, especially the rapid decay shown in SU1, should be discussed in the context of high precision human measurements of the geomagnetic field. The first measurement of field intensity was conducted by Carl Friedrich Gauss in 1832 [*Malin and Barraclough*, 1982]. Continuous measurements ever since allow spherical harmonic modeling of the field [e.g., *Jackson et al.*, 2000; *Finlay et al.*, 2010] and evaluation of the geomagnetic secular variation (SV) at any point on Earth. Here, we use the gufm1 model [*Jackson et al.*, 2000] from 1840 to 1990 and the IGRF models from 1990 to 2010 [*Finlay et al.*,

2010] to calculate for each location on Earth the relative % change in the geomagnetic field intensity ($100 \cdot \frac{B_{max} - B_{min}}{mean(B_{max}, B_{min})}$, where B_{min} and B_{max} are the endpoints B values in the selected time window—10 or 100 years). In each location, we find the maximum % change per decade and per century during the past 170 years (this time period is referred to as "the historical field" hereafter). Maps of the maximum % of change are displayed in Figure 9a (% per decade) Figure 9b (% per century). The maps show that the relative change on most of Earth's surface did not exceed 2.0 % per decade, and that most of the high temporal variability was concentrated in three confined lobes in the southern hemisphere: southeast and southwest of South Africa, and in South America. These lobes, when projected on Earth's core-mantle boundary are interpreted as dynamic flux patches, and it is their growth, migration, and expansion that produces the short-term variations observed on Earth's surface [*Gubbins*, 1987, *Jackson et al*., 2000, *Hulot et al*., 2002, *Gubbins et al*., 2006, *Olson and Amit*, 2006]. Interestingly, two of the active lobes in the southern hemisphere are paired with less active lobes at roughly the same longitude in the northern hemisphere: in the western Atlantic and the Middle East (our study area, which is marked with a triangle). The lobes with the highest rates of change in the historical field are marked with stars in Figures 9a and 9b. The intensity curves at the location marked with stars are shown in red in Figure 9c.

The archaeomagnetic data shown in Figure 6 have sufficient resolution to enable contextualization of the rates of change shown in Figure 9. We use the new data to address the question of whether the rates in the historical field represent typical characteristics of secular variation or, instead, indicate unusual behavior attributable to extreme events such as an immanent reversal as suggested by some researchers [e.g., *Olson*, 2002]. Our new data show that it is likely that relative change in Cyprus during the fifth century CE was of the order of the highest relative change in the historical field observed anywhere on Earth. In view of the new data and in agreement with recently published archaeomagnetic data (see below), the rapid intensity changes in the historical field should be interpreted as a normal phenomenon rather than an exceptional one.

This study complements recent archaeomagnetic studies that have suggested high temporal variability in the ancient field. *Gallet et al*. [2003] identified "archaeomagnetic jerks," short intervals of rapid changes in the direction of the field associated with intensity maxima apparent in the archaeomagnetic records of Europe and the Middle East. *Ben-Yosef et al*. [2009] and *Shaar et al*. [2011] reported short-lived high field anomalies during the Middle East Iron Age, referred to as "geomagnetic spikes". Other episodes with fast intensity changes of about 40% per century were reported in archaeointensity records from Western Europe [*Genevey et al*., 2009; *Gomez-Paccard et al*., 2012] and Eastern Europe [*Kovacheva et al*., 2009]. Thus, there is increasing evidence for high temporal variability in the ancient geomagnetic field. However, owing to the limited dating precision of most of the materials in the archaeomagnetic record (mostly of potsherds, baked clays, and volcanic rocks) and other sources of experimental uncertainties such as cooling rate effect in pottery [e.g., *Genevey et al*., 2008], subcentury-scale variations are inherently smoothed out in the compilation process of conventional archaeomagnetic data sets. Subcentury-scale variation that might be obscured in the available paleomagnetic records can be recovered using stratigraphically ordered high accumulation rate slag mounds, such as the ones studied here.

4.3. The Middle Eastern Geomagnetic Active Lobe

One interesting observation from Figure 9 is that significant changes in the geomagnetic field intensity do not occur randomly, and are instead concentrated in preferred locations. Assuming that the configuration of the geomagnetic field has not fundamentally changed over the past two millennia, we suggest that the rapid temporal variation observed in our study area (here, and in *Ben-Yosef et al*. [2009]; and *Shaar et al*. [2011]) is not coincidental. We suggest that the Middle Eastern area (triangle in Figure 9a) is the northern hemisphere mirror image of the presently active region south of Africa (star in Figures 9a). Together, the two areas may represent a closely related columnar convection structure. We conclude that at least one difference between the historical and the more ancient field is the level of activity in the northern hemisphere, which has been suppressed during the past centuries, but was significantly higher in the past.

5. Summary and Conclusions

We constructed two subcentury-scale paleointensity time series using ancient slag mounds from Cyprus—SU1 (fourth to fifth century CE, 25 m in height) and MK1 (seventh to fifth century BCE, 8 m in height). We established the accumulation chronology of SU1 using radiocarbon dates of short-lived organic materials

extracted from identified outer rings of small branches and twigs. The chronology of MK1 was difficult to obtain due to poor quality of charcoals. Absolute paleointensity estimates were obtained using Thellier-type IZZI experiments with anisotropy and nonlinear TRM assessments on georeferenced slag samples collected from different horizons in the mounds. The paleointensity analysis followed a recently published technique for automatic interpretation of paleointensity data, designed to minimize user-biased uncertainties attributed to subjective manual interpretation.

Overall, the Cypriot slag material behaved poorly in the paleointensity experiments and we reject more than 60% of the specimens based on low-quality Arai and Zijderveld plots. In addition, as the slag is very anisotropic, we reject specimens that failed the anisotropy correction procedure. Selected specimens that passed the strict paleointensity screening process were analyzed using electron microscopy and FORCs and confirmed the single-domain-like characteristics.

Twelve paleointensity estimates from MK1 indicate a relatively stable field during the time MK1 accumulated. In contrast, the paleointensity estimates from SU1 indicate a drop in field intensity during the fifth century CE. The relative change was likely to be higher than 2% per decade. To contextualize these findings, we analyzed the relative decadal change on Earth's surface during the past 170 years using the gufm1 and IGRF models, and found that relative changes comparable to SU1 occurred only in few confined locations: Central and South America, southern Atlantic, and South Africa. In most of Earth surface, the relative change did not exceed 2% per decade.

We suggest that the rapid temporal variation observed in the Levant (this study, *Ben-Yosef et al*., 2009; *Shaar et al*., 2011] is related to a Middle Eastern "activity lobe"—the northern hemispheric mirror image of the presently highly active region south of Africa. Together, this pair may represent a geomagnetic expression of a columnar convection structure within the liquid iron outer core.

The entire measurement data, the final interpretations, and the software to analyze the data (PmagPy Thellier GUI) are accessible from the MagIC database (http://earthref.org/MAGIC/) and from the PmagPy homepage (http://earthref.org/PmagPy/cookbook).

Acknowledgments

The authors wish to thank Mr. Constantinos Xydas, CEO of Hellenic Copper Mines Ltd., for his invaluable assistance during the excavations at Skouriotissa mines. We acknowledge the help of Matthew Vincent and Ashley Richter from Calit2, UCSD who operated the Total Station. We wish to thank the volunteers of the field expedition: Uri Davidovich, Jorge Perez, Philip Staudigel, Jennifer Roebber, and Alina Levy. We would like to thank Cathy Constable, Jeff Gee, Sanja Panovska, and Geoff Cromwell for constructive comments and suggestions. Jason Steindorf made most of the paleomagnetic measurements for this study. This work was funded by NSF grants EAR 0944137 to L.T. and T.E.L. and EAR 1141840 to L.T. We thank Pierrick Roperch and an anonymous reviewer for thorough reviews of an earlier version of the manuscript that significantly improved the current manuscript. We thank Adrian Muxworthy and David Heslop for their helpful review of the manuscript. Parts of this work were carried out in the Characterization Facility, University of Minnesota, which receives partial support from NSF through the MRSEC program. The authors dedicate this article to the memory of Hagai Ron, teacher, colleague, and friend.

References

Akkemik, Ü., and B. Yaman (2012), *Wood Anatomy of Eastern Mediterranean Species*, Kessel Publ. House, Remagen-Oberwinter.

Barraclough, D. R., J. G. Carrigan, S. R. C. Malin (2000), Observed geomagnetic field intensity in London since 1820, *Geophys. J. Int.*, *141*, 83–99, doi:10.1046/j.1365-246X.2000.00062.x.

Bastin, G. F., and H. J. M. Heijligers (1991), Quantitative electron probe microanalysis of ultra-light elements (boron-oxygen), in *Electron Probe Quantitation*, edited by K. J. F. Heinrich and D. E. Newbury, pp. 145–161, Plenum, N. Y.

Ben-Yosef, E., H. Ron, L. Tauxe, A. Agnon, A. Genevey, T. E. Levy, U. Avner, and M. Najjar (2008a), Application of copper slag in geomagnetic archaeointensity research, *J. Geophys. Res.*, *113*, B08101, doi:10.1029/2007JB005235.

Ben-Yosef, E., L. Tauxe, H. Ron, A. Agnon, U. Avner, M. Najjar, and T. E. Levy (2008b), A new approach for geomagnetic archaeointensity research: Insights on ancient metallurgy in the Southern Levant, *J. Archaeol. Sci.*, *35*, 2863–2879, doi:10.1016/j.jas.2008.05.016.

Ben-Yosef, E., L. Tauxe, T. E. Levy, R. Shaar, H. Ron, and M. Najjar (2009), Geomagnetic intensity spike recorded in high resolution slag deposit in Southern Jordan, *Earth Planet. Sci. Lett.*, *287*, 529–539, doi:10.1016/j.epsl.2009.09.001.

Ben-Yosef, E., R. Shaar, L. Tauxe, and H. Ron (2012), A new chronological framework for iron age copper production at Timna (Israel), *Bull. Am. Sch Orient. Res.*, *367*, 31–71.

Broadbent, C. P. (1987), Internal structure of solidified iron blast-furnace slag (BFS) droplets formed by self-impinging jets, *J. Mater. Sci. Lett.*, *6*, 1264–1266.

Bronk Ramsey, C. (2008), Deposition models for chronological records, *Quat. Sci. Rev.*, *27*, 42–60, doi:10.1016/j.quascirev.2007.01.019.

Bronk Ramsey, C. (2009), Bayesian analysis of radiocarbon dates, *Radiocarbon*, *51*, 337–360.

Bronk Ramsey, C., and S. Lee (2013), Recent and planned developments of the Program OxCal, *Radiocarbon*, *55*(2–3), 720–730.

Cafarella, L., A. Desantis, and A. Meloni (1992), Secular variation in Italy from historical geomagnetic-field measurements, *Phys. Earth Planet Inter. 73*, 206–221, doi:10.1016/0031-9201(92)90091-9.

Cartwright, C., and J. Parkington (1997), The wood charcoal assemblages from Elands Bay Cave, Southwestern Cape: Principles, procedures and preliminary interpretation, *South Afr. Archaeol. Bull.*, *52*, 59–72.

Coe, R. S., S. Gromme, and E. A. Mankinen (1978), Geomagnetic paleointensities from Radiocarbon-Dated lava flows on Hawaii and question of Pacific nondipole low, *J. Geophys. Res.*, *83*, 1740–1756, doi:10.1029/JB083iB04p01740.

Day, R., M. Fuller, and V. A. Schmidt (1977), Hysteresis properties of titanomagnetites grain- size and compositional dependence, *Phys. Earth Planet. Inter.*, *13*(4), 260–267, doi:10.1016/0031-9201(77)90108-X.

Dunlop, D. J. (2002), Theory and application of the Day plot (Mrs/Ms versus Hcr/Hc), 1. Theoretical curves and tests using titanomagnetite data, *J. Geophys. Res.*, *107*(B3), doi:10.1029/2001JB000486.

Dunlop, D. J., and Ö. Özdemir (2001), *Rock Magnetism: Fundamentals and Frontiers*, 573 pp., Cambridge Univ. Press., Cambridge, U. K.

Fahn, A., E. Werker, and P. Baas (1986), *Wood Anatomy and Identification of Trees and Shrubs from Israel and Adjacent Regions*, Isr. Acad. of Sci. and Hum., Jerusalem, Israel.

Ferk, A., R. Leonhardt, K.-U. Hess, S. Koch, R. Egli, D. Krása, and D. B. Dingwell (2014), Influence of cooling rate on thermoremanence of magnetite grains: Identifying the role of different magnetic domain states, *J. Geophys. Res.*, *119*, 1599–1606, doi:10.1002/2013JB010845.

Finlay, C. C., et al. (2010), International Geomagnetic Reference Field: The eleventh generation, *Geophys. J. Int.*, *183*, 1216–1230, doi: 10.1111/j.1365-246X.2010.04804.x.
Gallet, Y., A. Genevey, and V. Courtillot (2003), On the possible occurrence of 'archaeomagnetic jerks' in the geomagnetic field over the past three millennia, *Earth Planet. Sci. Lett. 214*, 237–242, doi:10.1016/S0012-821X(03)00362-5.
Gallet, Y., A. Genevey, M. Le Goff, F. Fluteau, and S. A. Eshraghi (2006), Possible impact of the Earth's magnetic field on the history of ancient civilizations, *Earth Planet Sci. Lett.*, *246*, 17–26, doi:10.1016/j.epsl.2006.04.001.
Genevey, A., and Y. Gallet (2002), Intensity of the geomagnetic field in western Europe over the past 2000 years: New data from ancient French pottery, *J Geophys. Res.*, *107*(B11), 2285, doi:10.1029/2001JB000701.
Genevey, A., Y. Gallet, C. G. Constable, M. Korte, and G. Hulot (2008), ArcheoInt: An upgraded compilation of geomagnetic field intensity data for the past ten millennia and its application to the recovery of the past dipole moment, *Geochem. Geophys. Geosyst.*, *9*, Q04038, doi:10.1029/2007GC001881.
Genevey, A., Y. Gallet, J. Rosen, and M. Le Goff (2009), Evidence for rapid geomagnetic field intensity variations in Western Europe over the past 800 years from new French archeointensity data, *Earth Planet Sci. Lett. 284*, 132–143, doi:10.1016/j.epsl.2009.04.024.
Genevey, A. S., Y. Gallet, and J. C. Margueron (2003), Eight thousand years of geomagnetic field intensity variations in the eastern Mediterranean, *J. Geophys. Res.*, *108*(B5), 2228, doi:10.1029/2001JB001612.
Gomez-Paccard, M., et al. (2012), Improving our knowledge of rapid geomagnetic field intensity changes observed in Europe between 200 and 1400 AD, *Earth Planet. Sci. Lett.*, *355*, 131–143, doi:10.1016/j.epsl.2012.08.037.
Gubbins, D. (1987), Mechanism for geomagnetic polarity reversals, *Nature*, *326*, 167–169, doi:10.1038/326167a0.
Gubbins, D., A. L. Jones, and C. C. Finlay (2006), Fall in Earth's magnetic field is erratic, *Science*, *312*, 900–902, doi:10.1126/science.1124855.
Halgedahl, S. L., R. Day, and M. Fuller (1980), The effect of cooling rate on the intensity of weak-field TRM in single-domain magnetite, *J. Geophys. Res.*, *85*, 3690–3698, doi:10.1029/JB085iB07p03690.
Harrison, R. J., and J. M. Feinberg (2008), FORCinel: An improved algorithm for calculating first-order reversal curve distributions using locally weighted regression smoothing, *Geochem. Geophys. Geosyst.*, *9*, Q05016, doi:10.1029/2008GC001987.
Hext, G. R. (1963), Estimation of second-order tensors, with related tests and designs, *Biometrika*, *50*, 353–373, doi:10.1093/biomet/50.3-4.353.
Hulot, G., C. Eymin, B. Langlais, M. Mandea, and N. Olsen (2002), Small-scale structure of the geodynamo inferred from Oersted and Magsat satellite data, *Nature*, *416*, 620–623, doi:10.1038/416620a.
Jackson, A., A. R. T. Jonkers, and M. R. Walker (2000), Four centuries of geomagnetic secular variation from historical records, *Philos. Trans. R. Soc. London A*, *358*, 957–990.
Jelinek, V. (1978), Statistical processing of aniosotropy of magnetic-susceptibility measured on groups of specimens, *Stud. Geophys. Geod.*, *22*, 50–62.
Kassianidou, V. (2004), Recording Cyprus's mining history through archaeological survey, *Brit. Sch. Athens Stud.*, 95–104.
Kirschvink, J. L. (1980), The least-squares line and plane and the analysis of paleomagnetic data, *Geophys J. R. Astron. Soc.*, *62*, 699–718, doi: 10.1111/j.1365-246X.1980.tb02601.x.
Kovacheva, M., A. Chauvin, N. Jordanova, P. Lanos, and V. Karloukovski (2009), Remanence anisotropy effect on the palaeointensity results obtained from various archaeological materials, excluding pottery, *Earth Planets Space*, *61*, 711–732.
Levy, T. E., et al. (2008), High-precision radiocarbon dating and historical biblical archaeology in southern Jordan, *Proc. Natl. Acad. Sci. U. S. A.*, *105*, 16,460–16,465, doi:10.1073/pnas.0804950105.
Malin, S. R. C., and D. R. Barraclough (1982), 150th anniversary of Gauss 1st absolute magnetic measurement, *Nature*, *297*, 285.
Manasse, A., and M. Mellini (2002), Chemical and textural characterization of medieval slags from the Massa Marittima smelting sites (Tuscany, Italy), *J. Cult. Herit.*, *3*(3), 187–198, doi:10.1016/S1296-2074(02)01176-7.
Min'ko N. I., V. A. Nevedomskii, and V. V. Vagin (1988), Crystallization in silicomanganese slag castings, *Glass Ceram.*, *45*(3), 114–116.
Nagata, T., K. Momose, and Y. Arai (1963), Secular variation of geomagnetic total force during last 5000 years, *J. Geophys. Res.*, *68*, 5277–5281.
Olson, P. (2002), Geophysics: The disappearing dipole, *Nature*, *416*.
Olson, P., and H. Amit (2006), Changes in earth's dipole, *Naturwissenschaften*, *93*, 519–542.
Paterson, G. A., D. Heslop, and A. R. Muxworthy (2010), Deriving confidence in paleointensity estimates, *Geochem. Geophys. Geosyst.*, *11*, Q07Z18, doi:10.1029/2010GC003071.
Paterson, G. A., L. Tauxe, A. J. Biggin, R. Shaar, and L. C. Jonestrask (2014), On improving the selection of Thellier-type paleointensity data, *Geochem. Geophys. Geosyst.*, *15*, 1180–1192, doi:10.1002/2013GC005135.
Pike, C. R., A. P. Roberts, and K. L. Verosub (1999), Characterizing interactions in fine magnetic particle systems using first order reversal curves, *J. Appl. Phys.*, *85*(9), 6660–6667.
Pouchou, J. L., and F. Pichoir (1984), New model for quantitative x-ray microanalysis. Part I: Application to the analysis of homogeneous samples [English Ed.], *Rech. Aerosp.*, *3*, 13–38.
Reimer, P. J., et al. (2013), Intcal13 and Marine13 radiocarbon age calibration curves 0–50,000 years Cal Bp, *Radiocarbon*, *55*, 1869–1887, doi:10.2458/azu_js_rc.55.16947.
Rogers, J., and J. M. W. Fox, and M. J. Aitken (1979), Magnetic-anisotropy in ancient-pottery, *Nature*, *277*, 644–646.
Schweingruber, F. H. (1990), *Anatomy of European Woods*, Paul Haupt, Bern and Stuttgart, Stuttgard.
Selkin, P. A., and L. Tauxe (2000), Long-term variations in palaeointensity, *Philos. Trans. R. Soc. A.*, *358*, 1065–1088, doi:10.1098/rsta.2000.0574.
Selkin, P. A., J. S. Gee, and L. Tauxe (2007), Nonlinear thermoremanence acquisition and implications for paleointensity data, *Earth Planet. Sci. Lett.*, *256*, 81–89, doi:10.1016/j.epsl.2007.01.017.
Selkin, P. A., J. S. Gee, L. Tauxe, W. P. Meurer, and A. J. Newell (2000), The effect of remanence anisotropy on paleointensity estimates: A case study from the Archean Stillwater Complex, *Earth Planet. Sci. Lett.*, *183*, 403–416, doi:10.1016/S0012-821X(00)00292-2.
Shaar, R., and J. M. Feinberg (2013), Rock magnetic properties of dendrites: Insights from MFM imaging and implications for paleomagnetic studies, *Geochem. Geophys. Geosyst.*, *14*, 407–421, doi:10.1002/ggge.20053.
Shaar, R., and L. Tauxe (2013), Thellier GUI: An integrated tool for analyzing paleointensity data from Thellier-type experiments, *Geochem. Geophys. Geosyst.*, *14*, 677–692, doi:10.1002/ggge.20062.
Shaar, R., H. Ron, L. Tauxe, R. Kessel, A. Agnon, E. Ben-Yosef, and J. M. Feinberg (2010), Testing the accuracy of absolute intensity estimates of the ancient geomagnetic field using copper slag material, *Earth Planet. Sci. Lett.*, *290*, 201–213, doi:10.1016/j.epsl.2009.12.022.
Shaar, R., E. Ben-Yosef, H. Ron, L. Tauxe, A. Agnon, and R. Kessel (2011), Geomagnetic field intensity: How high can it get? How fast can it change? Constraints from Iron Age copper slag, *Earth Planet. Sci. Lett.*, *301*, 297–306, doi:10.1016/j.epsl.2010.11.013.

Tauxe, L. (2010), Essentials of Paleomagnetism, 512 pp., Univ. of California Press, Berkeley, Calif.
Tauxe, L., and H. Staudigel (2004), Strength of the geomagnetic field in the Cretaceous normal Superchron: New data from submarine basaltic glass of the Troodos Ophiolite, *Geochem. Geophys. Geosyst.*, *5*, Q02H06, doi:10.1029/2003GC000635.
Tauxe, L., H. N. Bertram, and C. Seberino (2002), Physical interpretation of hysteresis loops: Micromagnetic modeling of fine particle magnetite, *Geochem. Geophys. Geosyst.*, *3*(10), 1055, doi:10.1029/2001GC000241.
Tauxe, L., and T. Yamazaki (2007), Paleointensities, in Treatise on Geophysics, Geomagnetism, vol. 5, edited by G. Schubert, pp. 509–564, Elsevier Ltd., Oxford, U. K.
Touchan, R., E. Xoplaki, G. Funkhouser, J. Luterbacher, M. K. Hughes, N. Erkan, U. Akkemik, and J. Stephan (2005), Reconstructions of spring/summer precipitation for the Eastern Mediterranean from tree-ring widths and its connection to large-scale atmospheric circulation, *Clim. Dyn.*, *25*, 75–98.
Valet, J. P. (2003), Time variations in geomagnetic intensity, *Rev. Geophys.*, *41*(1), 1004, doi:10.1029/2001RG000104.
Whitney, D. L., and B. W. Evans (2010), Abbreviations for names of rock-forming minerals, *Am. Mineral.*, *95*, 185–187.
Wyderko, M., and E. Mazanek (1968), The mineralogical characteristics of calcium-iron olivines, *Mineral. Mag.*, *36*, 955–961.
Zijderveld, J. D. (1967), *A.C. demagnetization of rocks, analysis of results, in Methods in Paleomagnetism*, edited by D. W. Collinson, K. M. Creer, and S. K. Runcorn, pp. 254–286, Elsevier, Amsterdam.